

The elliptic whistler jet

By HYDER S. HUSAIN AND FAZLE HUSSAIN

Mechanical Engineering Department, University of Houston, Houston, TX 77204-4792, USA

(Received 9 May 1997 and in revised form 10 May 1999)

Elliptic jets have decided advantages for technological applications over circular jets; this paper explores further advantages achieved by jet forcing due to self-excitation. Using hot-wire measurements and flow visualization, we have studied an elliptic whistler (i.e. self-excited) air jet of 2 : 1 aspect ratio which, in contrast to an elliptic jet issuing from a contoured nozzle, displays no axis switching, but significantly increased spread in the major-axis plane. Its near-field mass entrainment is considerably higher (by as much as 70%) than that of a non-whistling jet. Flow visualization reveals unexpected dynamics of the elliptic vortical structures in the whistler jet compared to that in the non-whistling jet. Vortices rolled up from the lip of the elliptic pipe impinge onto the collar, producing secondary vortices; interaction of these two opposite-signed vortices is shown to cause the different behaviour of the whistler jet.

1. Introduction

The whistler jet is a promising *passive* control device for technological applications such as mixing and combustion: it can produce self-excitation of controllable frequencies and amplitudes, it has a simple geometry, and it requires no external power for forcing. In this paper, we study elliptic whistler (pipe) jet vortex dynamics and their influence on mass entrainment. We compare this jet with the non-whistling pipe jet and also with an externally forced jet from a contoured nozzle. Hereinafter, we use the following abbreviations: WPJ – an elliptic whistler (pipe) jet (passively) excited by a collar; NPJ – a non-whistling jet issuing from an elliptic pipe without a collar; UCJ – an unexcited elliptic jet issuing from a contoured nozzle (with a top hat velocity profile); and ECJ – an elliptic jet from a contoured nozzle excited by external (active) forcing.

The WPJ configuration consists of an elliptic cross-sectional tailpipe attached to the downstream end of an elliptic nozzle with an elliptic collar sliding over the pipe (figure 1). The NPJ has the same configuration as the WPJ except that the collar is retracted, hence ineffective as a passive control device. In a WPJ, as the collar is pulled downstream (i.e. as the collar overhang L_c is increased), an audible single-frequency tone (associated with an exit velocity pulsation) abruptly appears. As L_c continues to increase, the tone frequency decreases monotonically, while the amplitude first increases, then reaches a peak, and then finally decays until it disappears; this is the first stage. As L_c is increased further, a second stage of excitation appears with a new (lower) frequency and then peaks and disappears in a similar fashion.

The whistler phenomenon (i.e. self-excitation) in a circular jet was first observed by Hill & Greene (1977). Hasan & Hussain (1979, 1982) showed that self-excitation in a circular whistler jet results from the coupling of two independent resonance mechanisms: (i) a shear layer tone, caused by the impingement of the pipe-exit shear

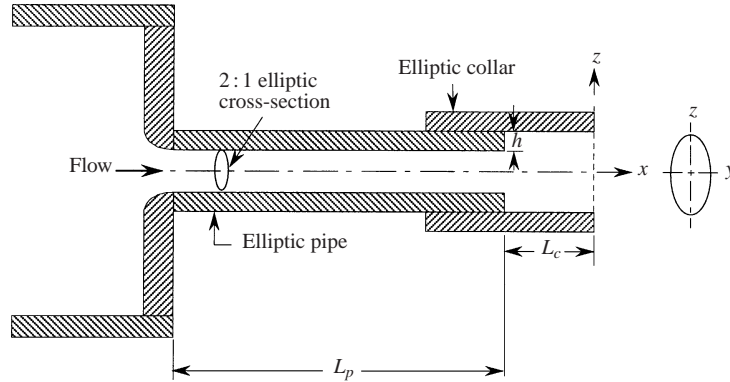


FIGURE 1. Schematic of the elliptic whistler nozzle details and coordinates.

layer on the collar, and (ii) the organ-pipe resonance in the tailpipe. A vortex formed from the roll-up of the shear layer downstream of the pipe exit impinges on the collar wall, resulting in a pressure fluctuation that propagates upstream, triggering the next vortex rollup at the pipe exit. Under the appropriate combinations of pipe length L_p , collar overhang L_c , pipe diameter D , step height h , and pipe exit velocity U_e , the frequencies of the two modes (shear layer tone and organ-pipe resonance) match; this resonance produces an enhanced excitation amplitude. Based on experimental data, Hasan & Hussain (1979) obtained an expression describing the dependence of the whistler frequency on L_c , L_p , D , the stage of excitation and the mode (namely half- and full-wave).

Husain & Hussain (1983) and Hussain & Husain (1989) found that UCJ and ECJ characteristics are quite different from planar and circular jets. Distinctive features include three-dimensional deformation of elliptic vortex rings due to curvature dependent self-induction causing axis switching and different jet spreads in the major- and minor-axis planes. Such vortex deformation, combined with properly chosen external forcing frequency and amplitude, can substantially alter jet evolution. Ho & Gutmark (1987) found that mass entrainment in a 2:1 unexcited elliptic jet was higher than that in a circular jet. Thus, (passive) jet control is possible through simple modifications of the nozzle geometry.

Our goal is to achieve further increase in mass entrainment via self-excitation in a WPJ. Specifically, our objectives are (a) to examine the effect of nozzle geometry on turbulence characteristics and on mass entrainment, and (b) to explain the vortex dynamics responsible for the experimental observations. To this end, we visualize the flow and measure jet characteristics (such as the jet spread, the coherent azimuthal vorticity, and mass entrainment).

Following a brief description of the jet facility and the experimental procedure (§2), we discuss the boundary layer characteristics at the pipe exit (§3.1). Section 3.2 addresses the frequency and amplitude variations of the jet tone with L_c . In §3.3, we discuss the time-averaged turbulence characteristics under excitation at the preferred mode frequency. Section 3.4 describes the flow visualization results. The modification of elliptic vortex ring dynamics due to the collar are addressed in §3.5. In §3.6, we discuss the deduced azimuthal coherent vorticity distributions in the minor- and major-axis planes. The mass entrainment measurements are discussed in §3.7.

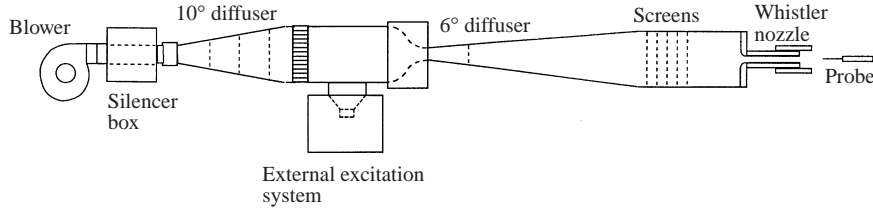


FIGURE 2. Schematic of the jet facility.

2. Experimental apparatus and procedure

2.1. Apparatus

Hot-wire measurements are made in an air jet facility (figure 2). A flexible rubber coupling, which connects the tunnel to a d.c. motor-driven centrifugal blower, isolates blower vibrations. The flow from the blower passes through a silencer box, a 10° conical diffuser, and a 5.08 cm deep honeycomb (hexagonal 3.2 mm cells) before entering the first of the two settling chambers. The flow then passes through a 7.62 cm contraction, a 6° conical diffuser, a second settling chamber, and five screens (mesh size 1.41 mm and screen wire diameter 0.178 mm), before exiting through an elliptic whistler nozzle into a large laboratory with controlled temperature and humidity.

Our studies of the UCJ and ECJ (Husain & Hussain 1983) revealed that the appropriate characteristic lengthscale is the equivalent diameter $D_e \equiv (ab)^{1/2}$, where a and b are the nozzle exit major- and minor-axis diameters respectively.

The current study uses an ASME profile nozzle of $D_e = 2.54$ cm and an aspect ratio $a/b = 2$. Elliptic holes matching the nozzle exit are milled into several Plexiglas plates (2.54 cm thick) which are then carefully aligned, glued, and sanded to form a smooth elliptic pipe. For this study, the values of L_p and h are kept fixed: $L_p = 30.38$ cm and $h = 0.32$ cm. In the NPJ the collar is retracted completely, i.e. $L_c = 0$. For the WPJ, data are taken for excitation at the preferred mode frequency.

Since a rolled-up elliptic vortex ring (and hence the jet cross-section) switches axes, references to local major- and minor-axis planes can be confusing. Therefore, we define *major-axis plane* to denote the reference plane containing the major axis at the pipe exit and the jet centreline; the *minor-axis plane* denotes the plane through the exit minor axis and the jet centreline. In addition, we refer to segments of a vortex intersecting these planes as *major-axis sides* and *minor-axis sides*. The x -axis origin is at the centre of the collar exit plane.

2.2. Measurement procedure

Time-average measurements

Data are taken with standard single and X-type hot wires (4 μ m tungsten wire with an effective length of approximately 2 mm) operating at an overheat ratio of 1.4 using AA Lab System constant-temperature anemometers. A MassComp MC5500 computer is used for traverse control, data acquisition, linearization, and data analysis. Hot-wire data are sampled in the differential mode with a 12-bit a/d converter. A two-channel digital Ono Sokki 920 spectrum analyser is used for spectra measurements.

Phase-average measurements

Azimuthal coherent vorticity in the major- and minor-axis planes are deduced at $x/D_e = 0.5$. Since the flow at this axial location is periodic, the signal from a

	Major axis (unexcited)	Minor axis (unexcited)	Major axis (excited)	Minor axis (excited)
δ^* (mm)	0.7	0.48	0.88	0.60
θ_e (mm)	0.3	0.21	0.56	0.35
H	2.33	2.27	1.58	1.71

TABLE 1. Initial conditions.

microphone (placed outside the collar slightly upstream from the exit plane) is used as the reference signal to obtain phase-averaged u - and v -velocities. At each transverse location, phase-averaging is performed using 1000 fundamental cycles, each cycle containing 100 data.

Phase-averaged velocities $\langle u \rangle$ and $\langle v \rangle$ are used to compute the coherent azimuthal vorticity $\langle \omega_z \rangle = -(1/0.5U_e)\partial\langle v \rangle/\partial t - \partial\langle u \rangle/\partial y$ distribution in (t, y) and (t, z) planes, i.e. in the minor- and major-axis planes. Note that in computing $\langle \omega_z \rangle$, the Taylor hypothesis has been invoked using a convection velocity of $0.5U_e$ (for details, see Zaman & Hussain 1981). $\langle \omega_z \rangle$ is non-dimensionalized by the preferred-mode self-excitation frequency f , given by $fD_e/U_e = 0.32$; time is non-dimensionalized by the fundamental cycle period, $T_c = 1/f$.

3. Results and discussion

3.1. Initial conditions

To facilitate the comparison of the turbulence characteristics of the WPJ with those of the circular whistler jet studied by Hasan & Hussain (1982), we have retained similar parameter ranges. For $U_e = 40.5 \text{ m s}^{-1}$, pure tone excitation (at $f = 515 \text{ Hz}$) in the first stage provides an excitation level of $u'_{fe}/U_e = 4.8\%$ (where u'_{fe} is the fundamental r.m.s. amplitude of the longitudinal velocity fluctuations at the nozzle exit centre). The values of U_e and f correspond to a Strouhal number $St_{De} (\equiv fD_e/U_e)$ of 0.32, the preferred mode of this elliptic jet.

Time-average measurements at the pipe-exit boundary layer characterize initial conditions. Figure 3(a,b) shows the mean and r.m.s. longitudinal velocity profiles at the elliptic pipe exit (about 0.5 mm downstream from the lip) for both the NPJ and WPJ ($St_{De} = 0.32$, $u'_{fe}/U_e = 4.8\%$). Table 1 gives the displacement thickness δ^* , momentum thickness θ_e , and shape factor H for the NPJ and WPJ.

High turbulence intensity in the boundary layer ($u'/U_e \geq 10\%$) and values of $H (< 2.59$ expected for laminar boundary layers) indicate that the boundary layers are transitional. Note that excitation thickens the mean velocity profile and renders it more turbulent-like (indicated by H -values).

3.2. Frequency and amplitude variation with collar length

To determine the preferred mode of the WPJ, self-excitation frequencies and amplitudes are measured for various L_c and U_e . While jet response can be investigated over a wide range of St_{De} with external forcing, there is only a small range of pure tone frequencies which can produce a large variation in u'_{fe}/U_e for self-excitation. For the nozzle used here, single-frequency self-excitation occurs for $U_e \geq 35 \text{ m s}^{-1}$; the maximum velocity is limited by the blower capacity to about 45 m s^{-1} . The first-stage

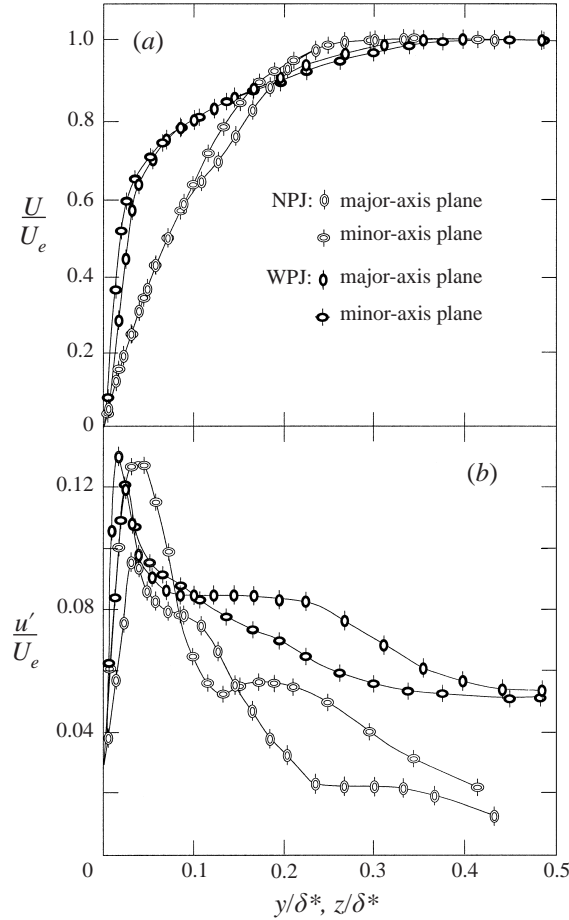


FIGURE 3. (a) Boundary layer mean velocity profiles at the elliptic pipe exit. (b) Longitudinal fluctuation intensity profiles at the elliptic pipe exit. $D_e = 2.54$ cm; $L_p = 30.48$ cm; $h = 0.32$ cm; $U_e = 40.5$ m s $^{-1}$. For the WPJ: $f = 515$ Hz; $St_{De} = 0.32$; $u'_{fe}/U_e = 4.8\%$.

frequencies lie in the 500–530 Hz range, corresponding to $0.28 \leq St_{De} \leq 0.38$ (for $D_e = 2.54$ cm).

For the preferred-mode determination, u'_{fe}/U_e must be kept approximately constant as St_{De} values are varied. To obtain a constant exit-plane excitation level at desired St_{De} values, both U_e (in the range 35–45 m s $^{-1}$) and L_c (in the range 1.2–1.5 cm) are adjusted. In the present case, u'_{fe}/U_e varies a little (4.6–4.8%) for the St_{De} range 0.28–0.37; outside this St_{De} range, u'_{fe}/U_e drops sharply. Thus, we search for the preferred mode within the above-mentioned St_{De} range.

For fixed L_p , U_e , D_e and h , the whistler phenomenon can be illustrated by examining the dependence of the excitation frequency f on L_c . As a typical example, we show the dependence of f and u'_{fe}/U_e on L_c in figure (4a, b) for two stages of self-excitation at $U_e = 40.5$ m s $^{-1}$. As in the circular jet, the pure-tone frequency in the first stage decreases monotonically with increasing L_c , disappears, then reappears and decreases again. The peak value of u'_{fe}/U_e (figure 4b) in the first stage is much higher (as much as about 4 times) than that in the second stage.

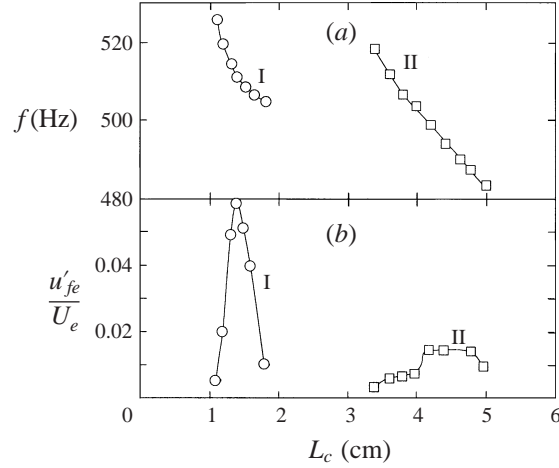


FIGURE 4. (a) Variation of whistler jet frequency with collar length L_c (cm). (b) Longitudinal turbulence intensity at the pipe exit. $h=0.32$ cm. $U_e=40.5$ m s $^{-1}$. \circ , First stage; \square , second stage.

3.3. Jet characteristics under excitation at the preferred mode

The preferred mode of a jet (Crow & Champagne 1971; Zaman & Hussain 1980; Gutmark & Ho 1983) is characterized by the dominant frequency observed near the end of the potential core in an unexcited flow. In an unexcited jet, the preferred mode frequency appears as a hump in the frequency spectrum because of phase jitter between successive structures. To clearly identify it, Zaman & Hussain (1980) defined the preferred mode as the frequency which produced the maximum growth of the *fundamental* r.m.s. amplitude u'_f along the centreline (by exciting at one frequency at a time); we have determined the WPJ preferred mode similarly.

Centreline turbulence intensity

The variations of the centreline longitudinal turbulence intensity $u'_c(x)$ and $u'_f(x)$ are shown in figure 5(a, b) for $St_{De} = 0.28, 0.3, 0.32, 0.33, 0.35$ and 0.37 for the WPJ and for the NPJ (i.e. $St_{De} = 0$). For measuring u'_f , the hot-wire signal is bandpass filtered with a 10% bandwidth around the fundamental frequency. The peak values of $u'_f(x)$ occur at $St_{De} = 0.32$; we choose $St_{De} \approx 0.32$ as the preferred mode frequency.

Centreline mean velocity decay

Figure 5(c) shows the centreline mean velocity decay U_c/U_e for the NPJ and WPJ for various St_{De} ; here U_c is the local mean centreline velocity. Excitation produces faster jet decay, presumably accompanied by higher entrainment (discussed later). Note that, under excitation, U_c shows a small decay for $x/D_e \approx 0$ to 2 and almost a plateau for $x/D_e \approx 2$ to 3.5.

Our studies of the UCJ, ECJ (Hussain & Husain 1989) and NPJ show the usual constant $U_c(x)$ up to $x/D_e \approx 4$ before U_c starts to decay. However, the WPJ shows, as does a whistler circular jet (Hasan & Hussain 1982), an initial decay, followed by an almost constant $U_c(x)$, and then the typical monotonic decay. Thus, it appears that this unusual character of early $U_c(x)$ decay is typical of whistler jets (excited by the collar). We will show (§3.5) that in the presence of a collar, a counter-rotating vortex is produced by the impingement of the primary vortex on the (non-slip) collar wall. It seems that the induced axial velocity due to the secondary vortex, which is directed opposite to that of U_c , is responsible for the initial decay (up to $x/D_e \approx 2$). From this

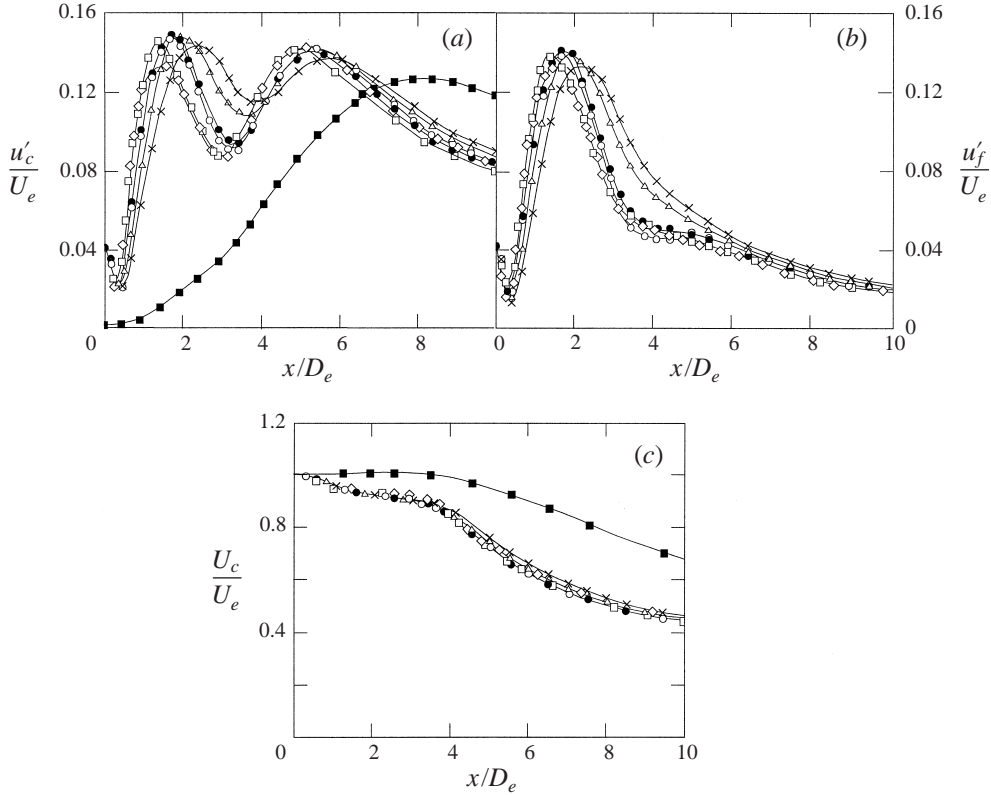


FIGURE 5. Dependence of (a) u'_c/U_e , (b) u'_f/U_e , and (c) U_c/U_e , on self-excitation. For the WPJ, St_{De} values are: \times , 0.28; Δ , 0.3; \bullet , 0.32; \circ , 0.33; \square , 0.35; \diamond , 0.37. For the NPJ: \blacksquare , $St_{De} = 0$.

location downstream, $U_c(x)$ exhibits the usual (collarless) jet behaviour, i.e. a plateau (up to $x/D_e \approx 3.5$) followed by monotonic decay.

Jet spread

We now examine the jet spread for the NPJ, WPJ, UCJ, and ECJ. Contours of U/U_c in the minor- and major-axis planes are shown in figure 6(a, b) for the WPJ and NPJ; jet half-widths, defined by the $U/U_c = 0.5$ line are shown in figure 6(c, d). For comparison, the equivalent jet half-width $B_e(\equiv (y_{0.5}z_{0.5})^{1/2})$ for all the jets is shown in figure 6(e).

U/U_c contours (figure 6a, b) show that self-excitation increases the jet spread, initially more in the major-axis plane, as indicated by arrows. Jet half-widths of the NPJ, UCJ and ECJ show that spreading in the minor-axis plane approaches and exceeds that in the major-axis plane, as is expected due to axis switching. Recall that three-dimensional deformation of an initially planar elliptic vortex ring leads to axis switching due to curvature-dependent non-uniform self-induction along the perimeter. Axis switching in the UCJ (with a thin boundary layer) occurs closer to the exit plane than in the NPJ because of a thicker, transitional boundary layer in the latter.

Recall that both the WPJ and ECJ were excited at the same $St_{De}(= 0.32)$ and $u'_{fe}/U_e(= 4.8\%)$. The ECJ shows the expected axis switching and an upstream shift in the switching location (compared to the UCJ; figure 6d). In contrast, the WPJ does not display axis switching (figure 6c). The jet half-width in the minor-axis plane

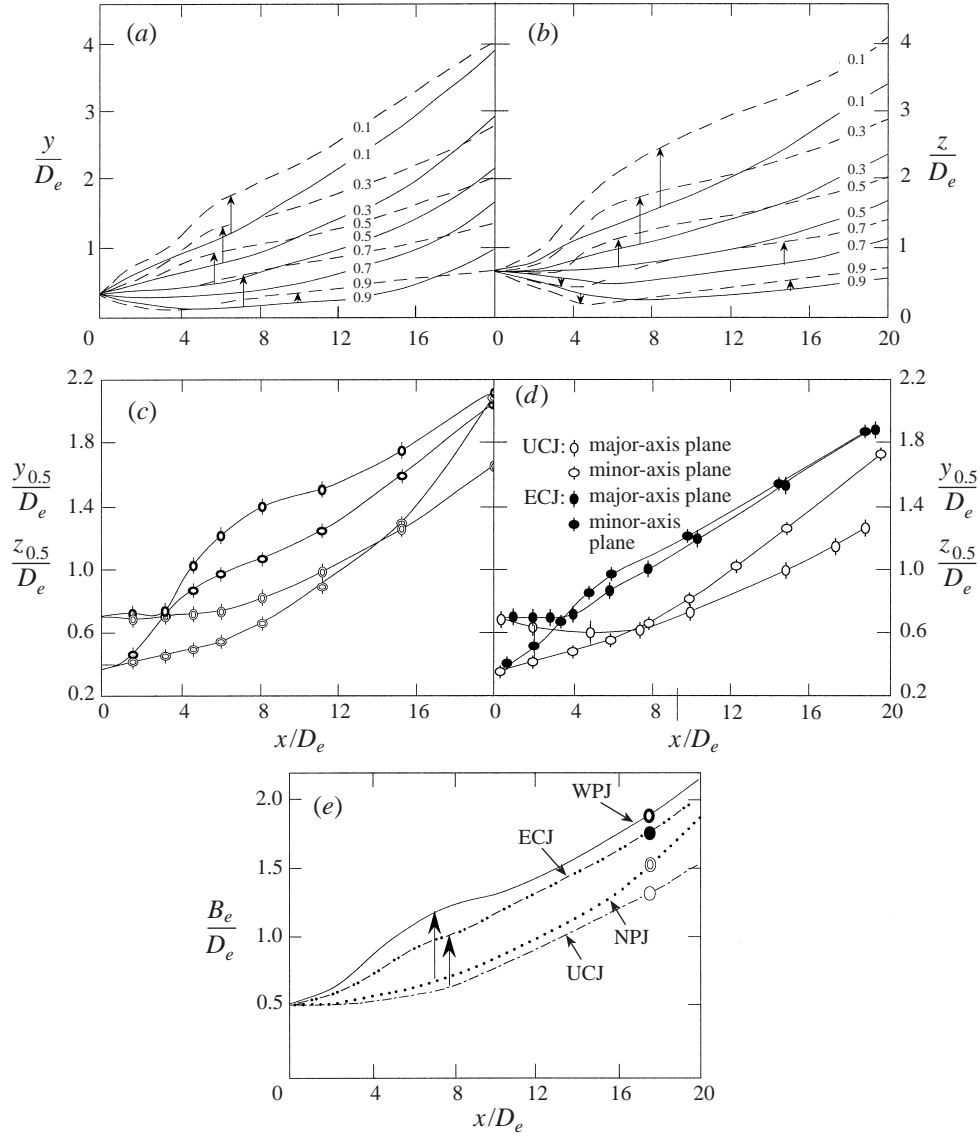


FIGURE 6. Contours of U/U_c : (a) minor-axis plane; (b) major-axis plane. —, NPJ; ----, WPJ. (c) Variations of jet half-widths of the NPJ and WPJ; symbols are the same as in figure 3. (d) Variations of jet half-widths of the UCJ and ECJ; $St_{De} = 0.32$; $u'_{je}/U_e = 4.8\%$. (e) Equivalent jet half-widths.

increases from the origin (i.e. the collar exit), while that in the major-axis plane shows almost no increase for $x/D_e \leq 3$ (figure 6c); at $x/D_e \approx 3$ the jet half-widths in both planes become comparable. For $x/D_e > 3$, there is no axis switching; instead, the jet half-width in the major-axis plane first grows at a much higher rate than that in the minor-axis plane up to about $x/D_e = 8$, then the rate decreases for $8 \leq x/D_e \leq 16$. Farther downstream (up to $D_e = 20$), the jet half-width growth rates in both planes become similar. Again, within the measurement range ($0 \leq x/D_e \leq 20$), no axis-

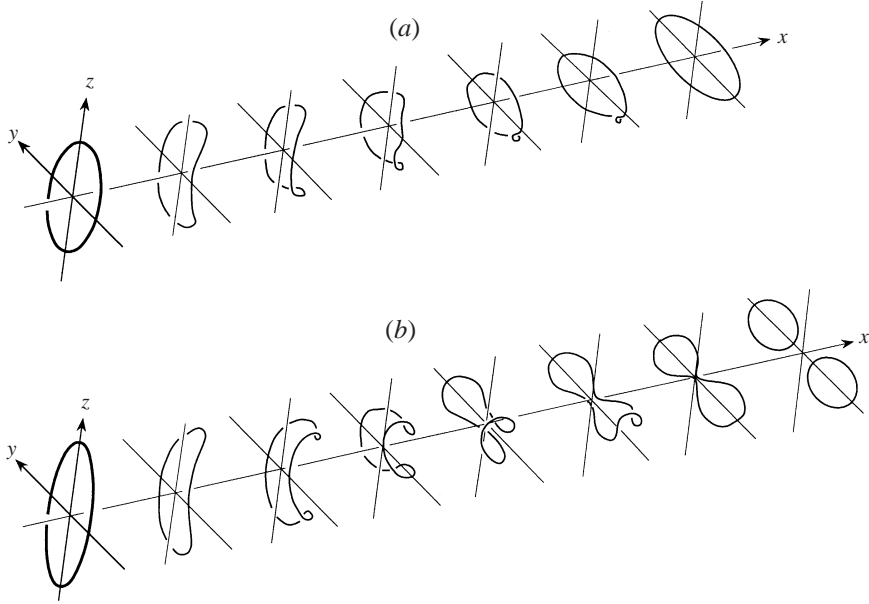


FIGURE 7. Schematics showing: (a) deformation and axis switching of a low-aspect-ratio elliptic vortex, and (b) deformation, axis switching and splitting (due to reconnection) of a high-aspect-ratio elliptic vortex.

switching occurs for the WPJ. While excitation (self or external) increases widths, the WPJ shows the highest jet spread, at all x/D , within the measurement range.

Variations of B_e show that the overall increase in the jet cross-sectional area reaches its maximum for the WPJ. For clarity, the increase in B_e due to excitation is indicated by arrows from the unexcited to the excited states (figure 6e).

The larger increase in the jet half-width of the WPJ even in the absence of axis switching is surprising. To understand this, we examine the dynamics of elliptic vortical structures under self/external excitations.

3.4. Flow visualization

Both axis switching and the splitting of elliptic vortex rings have been discussed in detail by Hussain & Husain (1989). For clarity, the deformation of elliptic rings leading to axis switching (for a low aspect ratio a/b) and splitting via vortex reconnection (for a high value of a/b) are shown schematically in figures 7(a) and 7(b) respectively. Briefly, the greater curvature (and hence, self-induced velocity) of the major-axis sides causes these sides to move ahead (and out of plane) of the minor-axis sides and toward the jet axis. This in turn produces greater curvature on the initial minor-axis sides, so that self-induction moves them away from the axis. Consequently, the initial minor axis of the ring now becomes the major axis, and vice versa. Elliptic vortex rings with a large aspect ratio (e.g. 4:1 ECJ; $St_{De} = 0.4$) display reconnection and split into two nearly circular rings, leading to jet bifurcation and enhanced spreading in the minor-axis plane (Hussain & Husain 1989). Here the major-axis sides (with a much higher curvature) come so close that they press against each other and the ring splits into two via vortex reconnection (figure 7b). Under the same excitation conditions, vortex rings in the 2:1 jet only switch axes without splitting (figure 7a).

Seeking an explanation for the absence of axis switching in the WPJ and the large jet width increase in the major-axis plane, we perform smoke flow visualization to examine the evolution of large-scale vortices in the presence of the collar. Using flow visualization to study vortex dynamics has intrinsic limitations since vorticity and marker diffusion rates can be quite different. More importantly, markers are depleted from regions of vorticity intensification by stretching so that dynamically significant events may escape observation. Thus, flow visualization must be applied and interpreted carefully or it can be misleading. In the present case, visualization is performed within the first 3–4 nozzle exit diameters at a jet speed of 40.5 m s^{-1} by introducing smoke at the exit plane. Since we study the vortical structures close to the marker injection location and the convective timescale is small compared to the diffusion timescale, we expect that marker distribution to accurately represent the vorticity field.

Smoke, cooled to room temperature, is injected slowly through 2 mm diameter tubes at the exit along the major and minor axes, without affecting the flow. The tube ends are about 5 mm away (radially) from the nozzle exit perimeter. Instantaneous structure cross-sections in each plane are captured on video. Since the flow is periodic, pictures in the two planes recorded at fixed phases but different times (by triggering the light strobing by a Wavetek phase-locked generator Model 80) can be regarded as simultaneous. The signal from a microphone is used for phase reference.

Phase-locked pictures of the whistler jet ($St_{De} = 0.32$, $u'_{fe}/U_e = 4.8\%$), exhibiting the evolution of structures in both major- and minor-axis planes, are shown in figure 8. The leading and trailing vortices are marked LV and TV respectively (frames *b1* and *b2*); the leading and trailing parts of the leading vortex in the minor-axis plane are marked LP and TP (frame *b1*).

Now we describe the evolution of vortices as observed via flow visualization; the flow is discussed in terms of vortex dynamics in the next subsection. The images reveal structures right at the collar exit. As a vortex exits from the collar, the minor-axis sides move toward the jet axis and touch each other at $x/D_e \approx 1.5$ (see the evolution of TV in frames *a1*–*i1*). This suggests vortex reconnection of nearby antiparallel vortex lines of the minor-axis sides (Melander & Hussain 1988). However, the resulting highly three-dimensional features (bridges and threads) are unlikely to be clear in the visualized pictures. Note that as the minor-axis sides approach the jet axis, the vortex cross-section is elongated in the axial direction (see TV in frames *a1*–*h1*) due to higher velocity on the jet axis. During this elongation, smoke is more concentrated near LP and TP than in the rest of the vortex (frame *b1*). When the minor-axis sides touch each other, the axial elongation is further enhanced (LV in frames *d1*–*h1*) due to head–tail formation (typical during reconnection). After the completion of reconnection, the newly formed vortices V1 and V2 (inclined to the jet axis in frame *i1*) move away from the jet axis by self-induction, producing increased spread. For clarity, the boundaries of reconnected vortices V1 and V2 are highlighted by solid lines.

Unlike the vortices in the UCJ or ECJ, the major-axis sides here move very little toward the jet; vortices LV and TV in the major-axis sides (frames *h2* and *i2*) are almost parallel to the jet centreline. Such behaviour of vortex evolution in both planes is consistent with the jet spread data (figure 6*d*).

For comparison, structure evolution in the ECJ ($St_{De} = 0.32$; $u'_e/U_e = 4.8\%$) is shown in figure 9. In this case, as expected, the shear layer rolls up at a location near $x/D_e \approx 0.3$; the structures in the minor- and major-axis planes move away from and toward the jet axis, respectively, by self-induction.

In the following subsection, we discuss the unusual vortex evolution in the WPJ and speculate on subsequent interactions that produce a significant increase in jet spread in the major-axis plane.

3.5. Vortex dynamics

As discussed in §3.4, axis switching occurs for an elliptic vortex ring when the major-axis sides move ahead of the minor-axis sides, producing curvature such that the minor-axis sides then move away from the centreline. In the WPJ, the question becomes: what causes the minor-axis sides to move towards the jet axis? This effect is found to be due to the impingement of vortices on the collar. As a vortex approaches a wall (e.g. Harvey & Perry 1971; Walker *et al.* 1987; and Orlandi 1990), it induces (at the wall) by no-slip, an intense thin vorticity layer which becomes unstable, rolls up into a secondary vortex of opposite sign, and causes the primary vortex to rebound by mutual induction. This effect explains the unexpected behaviour of WPJ rings.

As soon as an elliptic vortex ring forms near the pipe exit, the major-axis sides bend forward and toward the jet axis, while the minor-axis sides are pushed toward the collar wall (due to the curvature produced by the forward bending of the major-axis sides). This is schematically shown in figure 10(a). The motion of the minor-axis sides toward the collar wall produces a secondary vortex of opposite sign (shown schematically in figure 10b) similar to a vortex impinging on a non-slip wall. The two vortices form a dipole, which propels the minor-axis sides of the primary vortex toward the jet axis via mutual induction. Smoke fails to reveal distinct primary and secondary vortices downstream of the collar exit; however, the resultant inward motion of the vortex core (marked by concentrated smoke patches) is evident in the minor-axis plane (figure 8, vortex TV in frames *b1*, *c1*, *d1*, *e1* and *f1*). Note that, since the major-axis sides move away from the collar wall toward the jet axis, these sides cannot produce sufficiently high shear to induce a corresponding vortex rollup; the concentrated vortex lines in the induced secondary vortex on the minor-axis side, presumably fan out on to a sheet on the major-axis sides.

Time-averaged flow visualization

The dramatic variation in jet expansion is clearly seen via time-averaged flow visualization captured by a Minolta X-700 camera with a 6-s exposure time. In figure 11, we show visualized pictures of the NPJ (frames *a1* and *a2*), WPJ (frames *b1* and *b2*), UCJ (frames *c1* and *c2*), and ECJ (frames *d1* and *d2*). It is evident that the highest spread (hence entrainment) occurs in the WEJ. Because of smoke dilution, pictures cannot capture the jet boundaries correctly as the flow evolves. For the WPJ and ECJ, the slope of the jet boundaries, as marked by smoke, are indicated in the figures. The slopes of the WPJ in both planes correspond well with the slopes of the outermost contours in figure 6(a, b).

Jet bifurcation

Hot-wire data as well as phase-locked and time-averaged visualization indicates that jet bifurcation (figure 12a, b) occurs in both the WPJ and ECJ, but in different planes. In the WPJ, bifurcation (figure 12a) occurs across the minor-axis plane, while in the ECJ, bifurcation (figure 12b) occurs across the major-axis plane. Moreover, jet bifurcation occurs only at higher aspect ratios and higher excitation levels in the ECJ than that in the WPJ. (For details of jet bifurcation in a 4:1 ECJ, see Hussain & Husain 1989.)

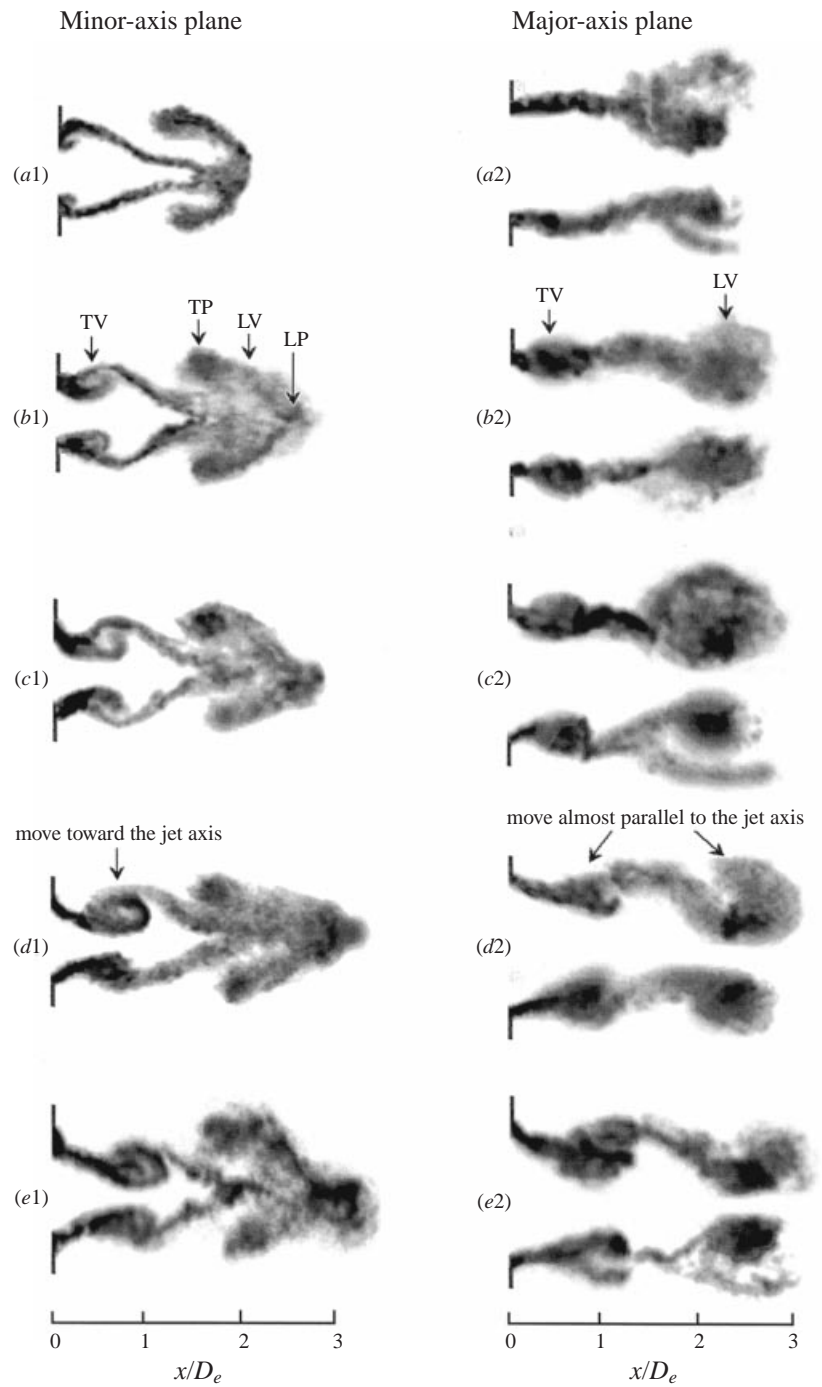


FIGURE 8 (a-e). For caption see facing page.

3.6. Vorticity distribution

To examine our conjecture of the generation of a counter-rotating vortex, we examine the evolution of centreline u_c -spectra, u - and v -signals, and deduce azimuthal coherent vorticity in both major- and minor-axis planes at $x/D_e = 0.5$.

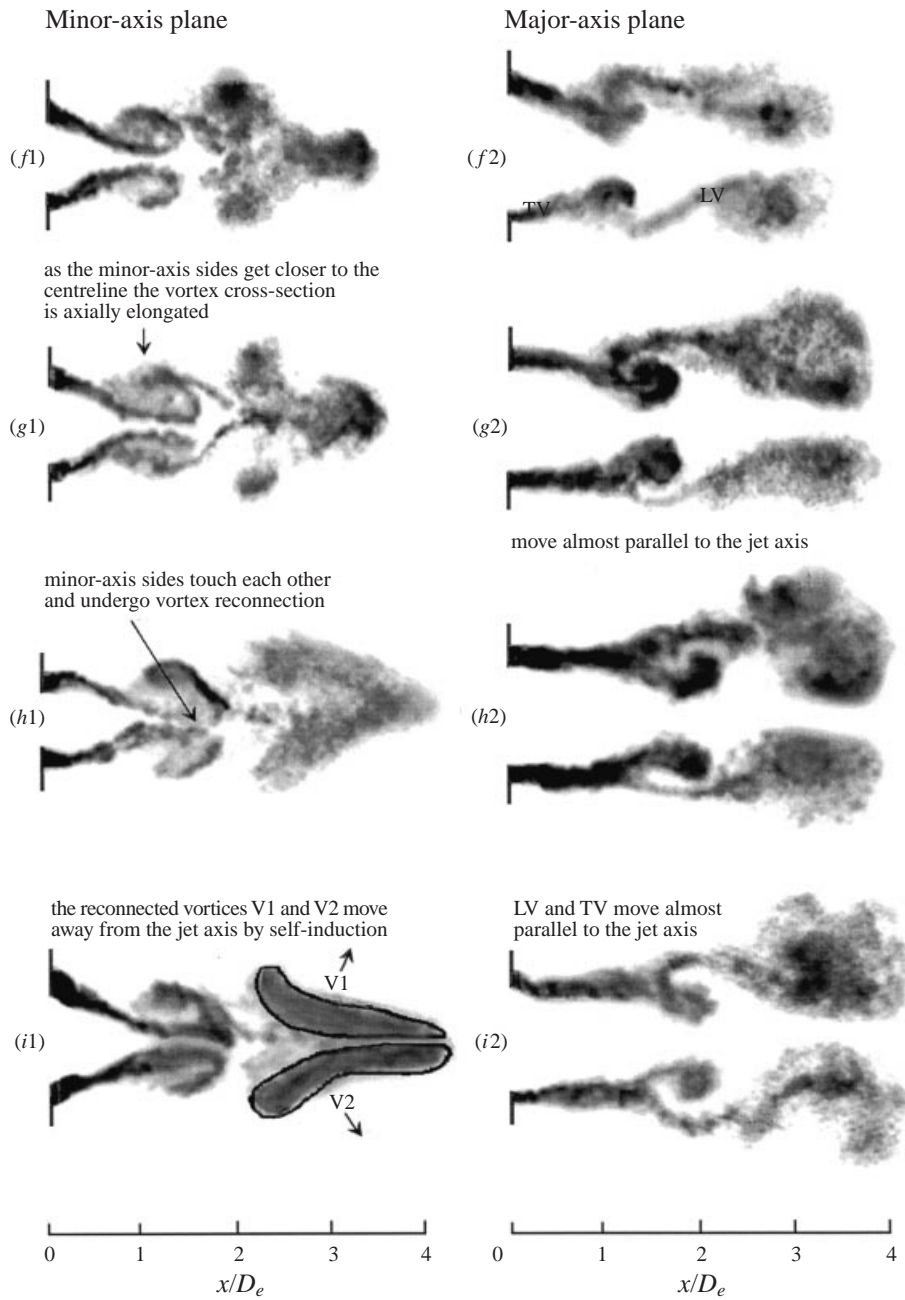


FIGURE 8. Instantaneous phase-locked visualization pictures showing the evolution of structures in the minor- and major-axis planes of the WPJ. $St_{De} = 0.32$; $u'_{fe}/U_e = 4.8\%$. In frame (i1), solid lines suggest boundaries of reconnected vortices V1 and V2.

Spectral evolution

Figure 13 shows streamwise evolution of $u_c(t)$ spectra; all these traces have the same logarithmic ordinate and linear abscissa scales. The spectra were averaged over 256 realizations with a frequency resolution of 0.25% of the maximum (i.e. 2000 Hz in

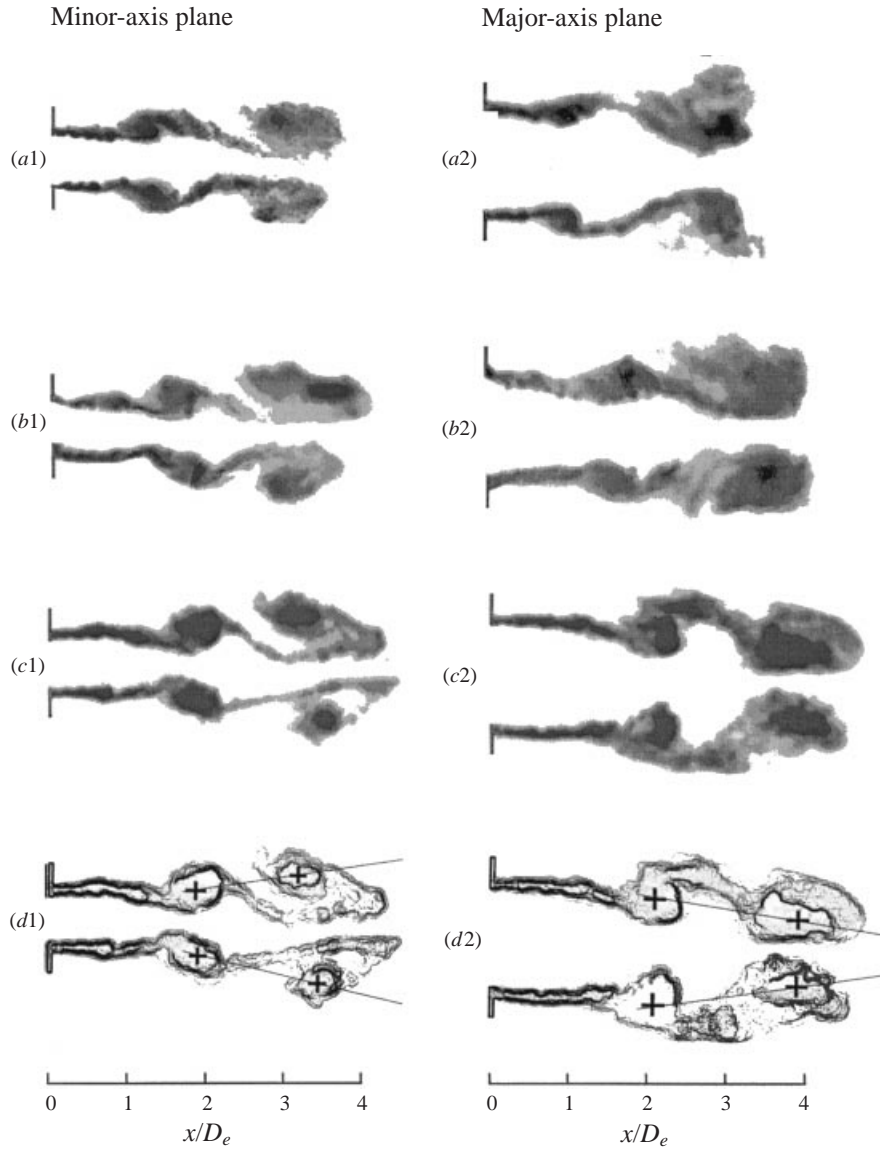


FIGURE 9. Instantaneous phase-locked visualization pictures showing the evolution of structures in the minor- and major-axis planes of the ECJ. $St_{D_e} = 0.32$; $u'_{fe}/U_e = 4.8\%$. Figures (d1, d2) represent boundaries of structures in (c1, c2), respectively, showing radial motions.

the present case). At the exit plane, the perturbation is almost sinusoidal; there are no discernible higher harmonics in the spectrum. Downstream of the exit plane, higher harmonics begin to grow rapidly. Near $x/D_e \approx 1.5$, both the fundamental and the first harmonic reach their peak values. Farther downstream, all peaks begin to decay. Beyond $x/D_e \approx 4.5$ the spectrum is fully developed and devoid of any noticeable spectral peak. This is by no means an indication of turbulence being fine-grained beyond $x/D_e \approx 4.5$; organized structures are in a state of large-scale breakdown; they lose their phase coherence, giving no discernible spectral footprint. In addition, vortex

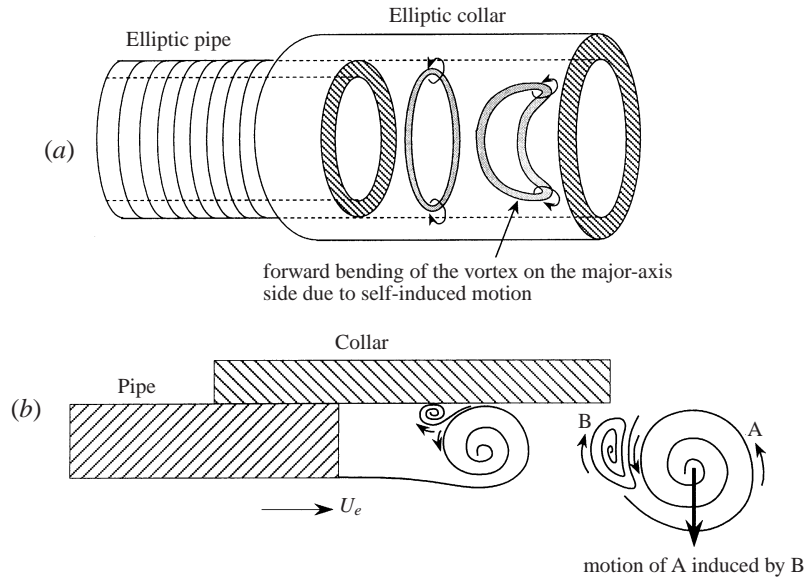


FIGURE 10. Schematics showing: (a) the deformation of an elliptic vortex ring inside the collar of the WPJ; (b) the formation of the secondary vortex B induced by primary vortex A.

reconnection is expected to occur near $x/D_e = 4$; this leads to small-scale generation and spatial and temporal jitters causing spectral broadening.

Interpretation of u - and v -signals

Before elucidating the coherent structure, we examine u - and v -signals and infer possible vortex configurations corresponding to these signals. Figures 14(a)–14(c) respectively show: (a) the u -signal at $x/D_e = 0.5$, $y/D_e = 0$; (b) the u -signal at $x/D_e = 0.5$, $y/D_e = 0.3$; and (c) the schematic of the pair of same-signed vortices that produce the segment of u -signal highlighted by a thick line in figure 14(b). Figure 14(a) shows a periodic u -signal; however, the off-axis u -signal shows two clear peaks in one fundamental cycle, indicating two vortices generated from a single fundamental vortex. The vortex configuration shown schematically in figure 14(c) will induce, along the dashed line shown, the u -signal at the bottom of figure 14(c); this signal pattern is very similar to that in figure 14(b). These two vortices are generated by tearing of the primary vortex ring into two (Monkewitz 1988); see hot-wire data in figure 15.

Figures 14(d)–14(f) respectively show: (d) the v -signal at $x/D_e = 0.5$, $y/D_e = 0$; (e) the v -signal at $x/D_e = 0.5$, $y/D_e = 0.3$; and (f) the schematic of the upstream primary vortex combined with a downstream secondary opposite-signed vortex that together produce the segment of v -signal highlighted by the thick line in figure 14(e).

As expected, the v -signal is almost zero (except for noise) at the centreline. The off-axis signal shows two peaks in one fundamental cycle (figure 14e). These two peaks are produced by the induced v -velocities, one by a stronger primary vortex, the other by a weaker downstream secondary vortex. The induced velocity signal along the dashed line in figure 14(f) is schematically shown at the bottom of figure 14(f), which is similar to the measured v -signal in figure 14(e).

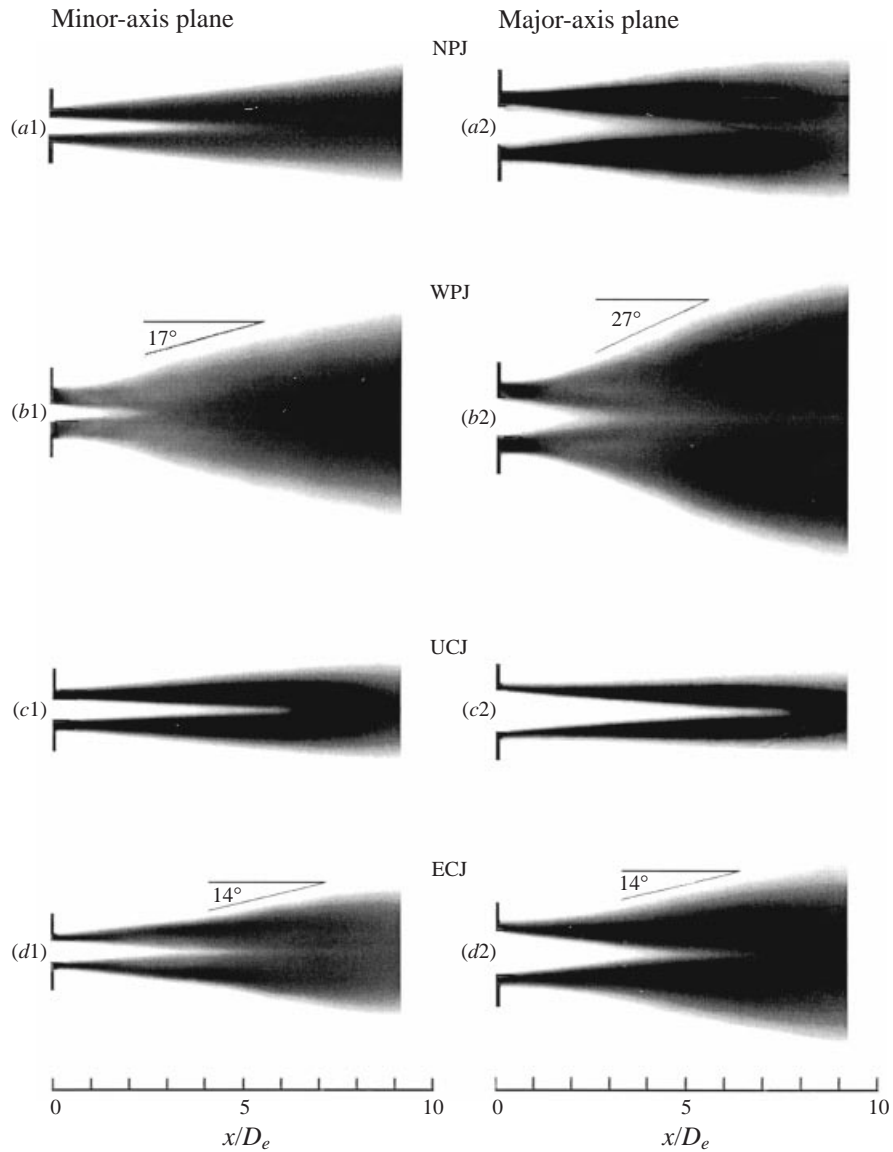


FIGURE 11. Time-averaged smoke visualization pictures.

Coherent vorticity

To quantitatively confirm the presence of secondary vortex and the tearing of the fundamental vortex, coherent vorticity at $x/D_e = 0.5$ is deduced. Periodicity of the flow at this location (as observed from the u -spectrum) allows us to use a simple deduction scheme employing a reference trigger signal for phase averaging. We use the signal from a microphone attached outside the nozzle, slightly upstream of the exit plane, as phase reference. Samples of u - and v -signals (1000 samples each) of the fundamental wavelength are aligned for phase averaging when the trigger signal crosses the zero level with a negative slope.

Contours of coherent azimuthal vorticity $\langle \omega_z \rangle / f$ in the minor- and major-axis

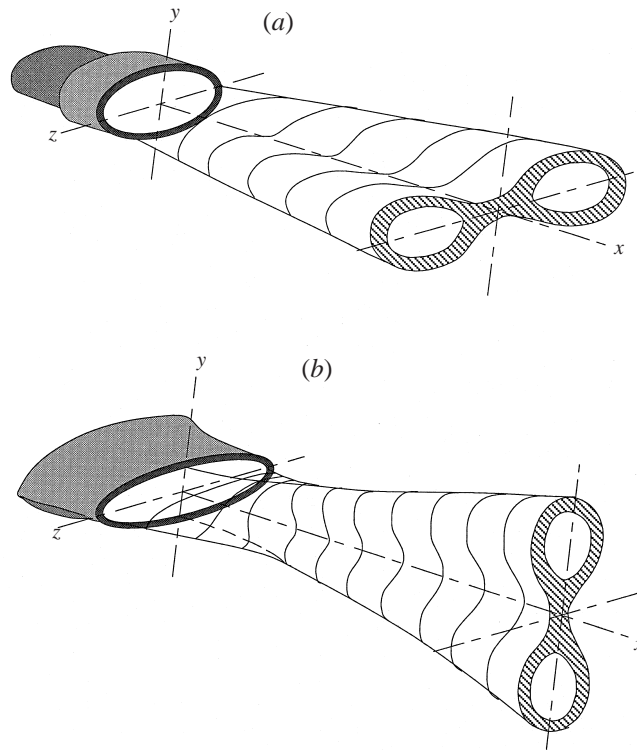


FIGURE 12. Schematics of the jet bifurcation: (a) 2:1 WPJ; (b) 4:1 ECJ.

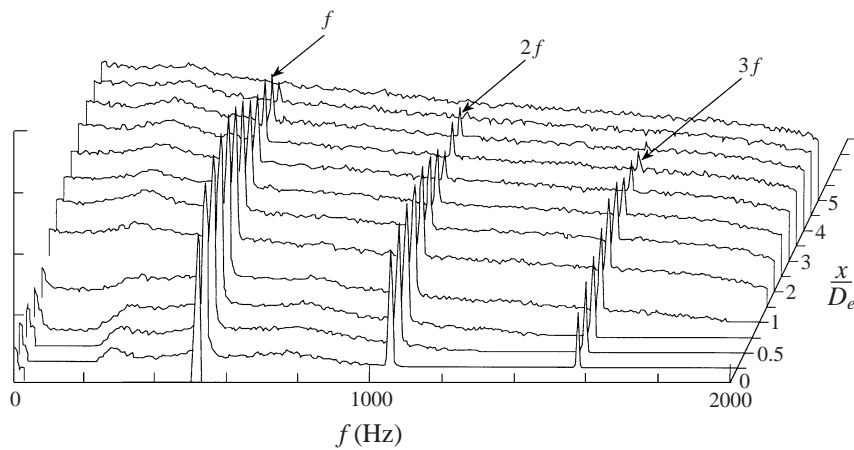


FIGURE 13. Evolution of the u -spectrum along the jet centreline of the WPJ.

planes are shown in figure 15(a, b). Note that the flow is from left to right in figure 15 since space and time are in opposite directions.

Positive vortices show two peaks (marked A1 and A2) and there is a downstream negative vortex (marked B). Vortex B was originally formed between the collar wall and the primary vortex A. The weaker vortex B is advected around vortex A (which is stronger and bigger) and occupies a downstream location in the captured phase. During this interaction of two opposite-signed vortices, the primary vortex A

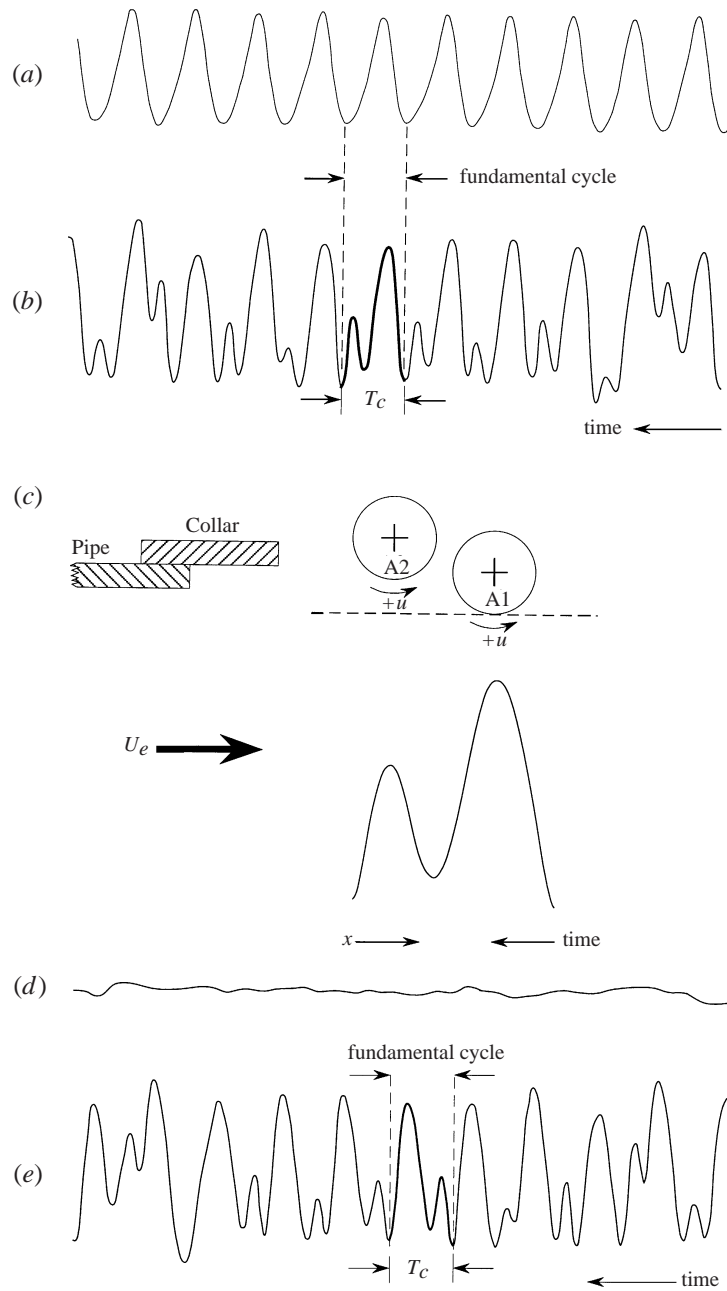


FIGURE 14 (a-e). For caption see facing page.

undergoes tearing producing two vortices, A1 and A2, where vortex A1 moves toward the jet axis. At this location the peak vorticity of B is almost one-fourth of vortex A1 or A2.

In the major-axis plane, the axial elongation of the vorticity contours is consistent with the visualized pictures in this plane. The size of the secondary vortex and its peak magnitude are much smaller in the major-axis plane than in the minor-axis

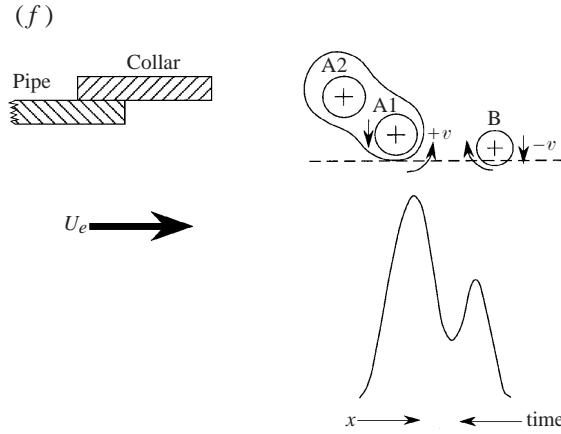


FIGURE 14. Velocity signal in WPJ: (a) u -signal at $x/D_e = 0.5$, $y/D_e = 0$; (b) u -signal at $x/D_e = 0.5$, $y/D_e = 0.3$; (c) schematic of vortex configuration that produces the u -signal in (b); (d) v -signal at $x/D_e = 0.5$, $y/D_e = 0$; (e) v -signal at $x/D_e = 0.5$, $y/D_e = 0.3$; (f) schematic of vortex configuration that produces the v -signal in (e).

plane, which confirms that forward bending of the major-axis side within the collar produces low near-wall shear and hence a much weaker counter-rotating vortex.

3.7. Effect of self-excitation on mass entrainment

In this subsection we examine the effect of self-excitation on mass entrainment in the WPJ and compare it with that in the circular jet. Radial profiles of the mean velocity are measured at intervals of 15° in one quadrant of the elliptic cross-section. The data at large radii, i.e. at locations of low U/U_c , are smoothed by fitting them with an exponential curve of the form $U/U_c = \exp(-br^2)$. This analytical expression is then used to generate data at farther outer radii where large fluctuation intensities and flow reversal render hot-wire measurements inaccurate (Chevray & Tutu 1978). Integration was carried out up to the location $y_{0.01}$, where $U/U_c = 0.01$ (also see Hasan & Hussain 1982).

Streamwise variations of mass entrainment E , defined as $E \equiv (Q - Q_0)/Q_0$, are shown in figure 16(a). Here Q and Q_0 denote local and exit-plane mass fluxes respectively; for comparison, circular whistler jet data (Hasan & Hussain 1982) are also shown.

The WPJ shows a significant increase in mass entrainment between $4D_e$ and $6D_e$, with a peak at $6D_e$ representing approximately a 70% increase in mass entrainment over that for the NPJ. Both the NPJ and WPJ have higher mass entrainments than those for circular pipe and whistler jets up to $x/D_e \approx 5$; in fact, irrespective of the presence or absence of excitation, the elliptic jets display enhanced mass entrainment in the near region ($x/D_e \leq 5$). The three-dimensional deformation, intrinsic to turbulent elliptic vortex rings, causes higher mass entrainment than in a circular jet (Husain & Hussain 1993); reconnection in the elliptic rings presumably increases entrainment further.

Ho & Gutmark's (1987) data (for an unexcited elliptic jet) show higher mass entrainment than that for the NPJ. In their case, it appears that the jet had an initially thin laminar boundary layer, initiating roll-up of thin-core vortices closer to the exit plane and hence faster deformation by self-induced motion. This early initiation of three-dimensionality could explain their observation of increased mass

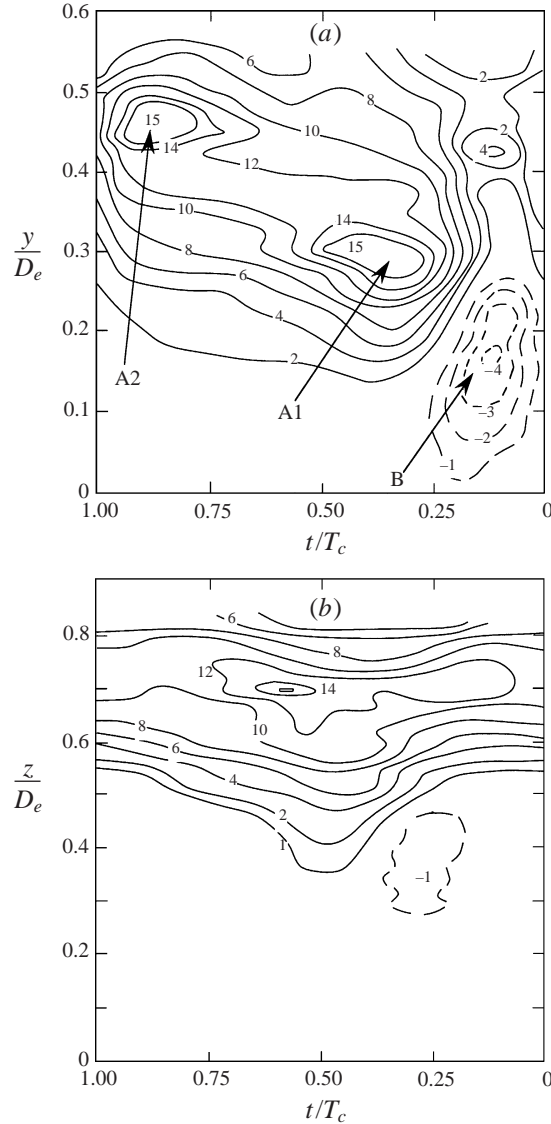


FIGURE 15. Contours of coherent azimuthal vorticity $\langle \omega_z \rangle / f$ for the WPJ: (a) minor-axis plane; (b) major-axis plane.

entrainment. In contrast, for an initially transitional or turbulent boundary layer jet, the rolled-up vortex core is thicker, causing less intense deformation and axis switching to occur farther downstream (Hussain & Husain 1989), thus resulting in decreased mass entrainment.

The WPJ shows a lower mass entrainment for $1 \leq x/D_e \leq 4$ than that measured by Ho & Gutmark (1987). However, between $D_e = 4$ and 8, the WPJ displays higher mass entrainment. This is to be expected because of the different vortex dynamics in the WPJ.

The mass entrainment rate, dE/dx' (where $x' = x/D_e$) as a function of x' , for the various kinds of elliptic jets, including Ho & Gutmark's (1987) elliptic jet are shown in figure 16(b) for comparison. Initially, dE/dx' for the WPJ decreases (to even less

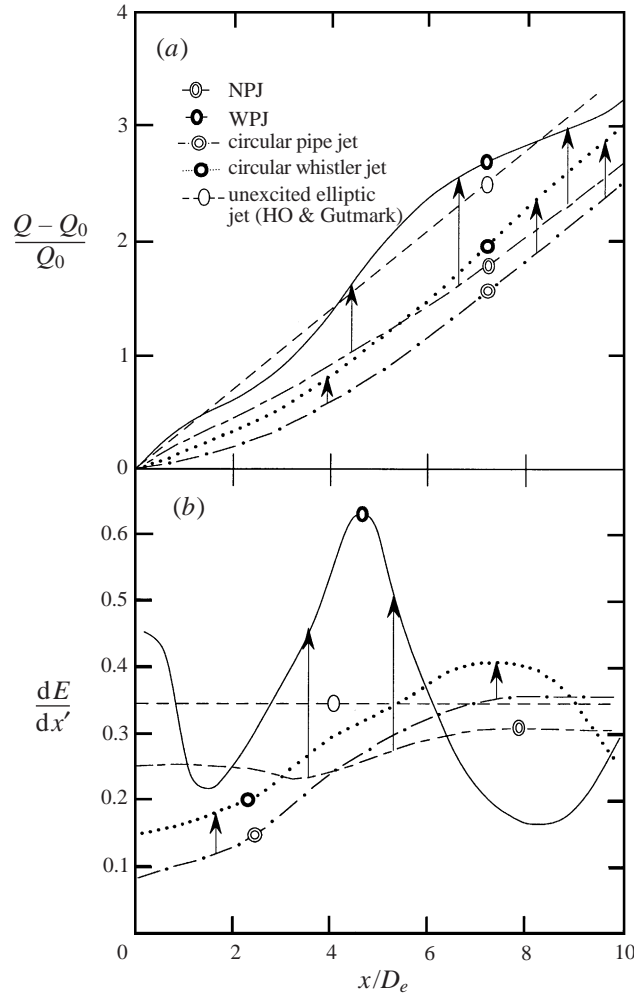


FIGURE 16. Variations of (a) mass entrainment and (b) entrainment rate with x .

than the level of the unexcited case) until $x/D_e \approx 1.5$ (perhaps because of rapid inward motion on the minor-axis sides). For $x/D_e \geq 1.5$, however, dE/dx' instead increases sharply and peaks near $x/D_e \approx 4.5$. At this location, dE/dx' is about 2.5 times that for the NPI.

4. Concluding remarks

Turbulence control is feasible only in the presence of coherent structures, i.e. no coherent structures, no control. The control methods may, in general, be classified as: (a) *active*—requiring external energy (typically by excitation), and (b) *passive*—requiring no external forcing. The latter can be achieved by initial condition and/or geometry modification, or by self-excitation. In this study we have explored passive control using geometry modifications, as well as via self-excitation in an elliptic pipe jet with a collar.

The effect of the collar is to significantly change the vortex dynamics via the generation of the secondary, counter-rotating vortex, which in turn induces the tearing of the

primary vortices. The leading part of the vortex moves toward the jet axis and undergoes vortex reconnection, while the trailing part moves away from the jet axis; these events, initiated by the secondary vortex, produce a significant increase in the jet spread and mass entrainment, which could not be attained in circular or elliptic jets without a collar. Our results suggest promising technological applications of the WPJ for enhancing near-field transport phenomena such as heat, mass, and momentum transfer.

For a rigorous study of the three-dimensional dynamics in such a jet, it is necessary to have complete spatial information at successive phases of the jet evolution. No existing numerical or experimental technique can provide this information at practical Reynolds numbers. Currently, direct numerical simulations and holographic particle velocimetry are limited to much lower Reynolds numbers and small flow regions. Despite such limitations, we have demonstrated that careful flow visualization can provide qualitative but significant information. Complementary use of flow visualization and limited time- and phase-averaged hot-wire measurements have revealed the essential vortex dynamics of the WPJ.

The authors are grateful to Sukesh Roy for helping in acquiring phase-averaged data, and to Dhoorjaty Pradeep for a careful review of the manuscript. This work was supported by Texas ARP Grant 003652-151.

REFERENCES

- CHEVRAY, R. & TUTU, N. K. 1978 Intermittency and preferential transport of heat in a round jet. *J. Fluid Mech.* **88**, 133.
- CROW, S. C. & CHAMPAGNE, F. H. 1971 Orderly structure in jet turbulence. *J. Fluid Mech.* **48**, 547.
- GUTMARK, E. & HO, C. M. 1983 Preferred modes and the spreading rates of jets. *Phys. Fluids* **26**, 2932.
- HARVEY, J. K. & PERRY, F. J. 1971 Flow field produced by trailing vortices in the vicinity of the ground. *AIAA J.* **9**, 1659.
- HASAN, M. A. Z. & HUSSAIN, A. K. M. F. 1979 A formula for resonance frequencies of a whistler nozzle. *J. Acoust. Soc. Am.* **69**, 1140.
- HASAN, M. A. Z. & HUSSAIN, A. K. M. F. 1982 The self-excited axisymmetric jet. *J. Fluid Mech.* **115**, 59.
- HILL, W. G. & GREENE, P. R. 1977 Increased turbulent jet mixing rates obtained by self-excited acoustic oscillation. *Trans. ASME I: J. Fluids Engng* **99**, 520.
- HO, C. M. & GUTMARK, E. 1987 Vortex induction and mass entrainment in a small-aspect ratio elliptic jet. *J. Fluid Mech.* **179**, 383.
- HUSAIN, H. S. & HUSSAIN, A. K. M. F. 1983 Controlled excitation of elliptic jets. *Phys. Fluids* **26**, 2763.
- HUSAIN, H. S. & HUSSAIN, F. 1993 Elliptic jets. Part 3. Dynamics of preferred mode coherent structure. *J. Fluid Mech.* **248**, 315.
- HUSSAIN, F. & HUSAIN, H. S. 1989 Elliptic jets. Part 1. Characteristics of unexcited and excited jets. *J. Fluid Mech.* **208**, 257.
- MELANDER, M. V. & HUSSAIN, F. 1988 Cut-and-connect of two antiparallel vortex tubes. *NASA-Stanford CTR Rep.* CTR-88, p. 257.
- MONKEWITZ, P. A. 1988 Subharmonic resonance, pairing and shredding in the mixing layer. *J. Fluid Mech.* **188**, 223.
- ORLANDI, P. 1990 Vortex dipole rebound from a wall. *Phys. Fluids A* **2**, 1429.
- WALKER, D. A., SMITH, C. R., CERRA, A. W. & DOLIGALSKI, T. L. 1987 The impact of a vortex on a wall. *J. Fluid Mech.* **181**, 99.
- ZAMAN, K. B. M. Q. & HUSSAIN, A. K. M. F. 1980 Vortex pairing in a circular jet under controlled excitation. Part 1. General response. *J. Fluid Mech.* **101**, 449.
- ZAMAN, K. B. M. Q. & HUSSAIN, A. K. M. F. 1981 Taylor hypothesis and large-scale coherent structures. *J. Fluid Mech.* **112**, 379.